# Reverse order-disorder transition of Janus particles confined in two dimensions

Yihao Liang,[1,2] Boran Ma,[2,*] and Monica Olvera de la Cruz[1,2,†]
[1]*Department of Physics and Astronomy, Northwestern University, Evanston, Illinois 60208, USA*
[2]*Department of Materials Science and Engineering, Northwestern University, Evanston, Illinois 60208, USA*

(Received 11 December 2020; accepted 3 May 2021; published 9 June 2021)

Janus particles with different patch sizes, confined to two dimensions, generate a series of patterns of interest to the field of nanoscience. Here we observe reverse melting, where for some densities the system melts under cooling. For a broad range of hydrophobic patch sizes ($60^\circ < \theta_0 < 90^\circ$), a reentrant transition from solid to liquid and then to an ordered phase emerges as temperature ($T$) decreases due to the formation of rhombus chains at low $T$. This reentrant phase has pseudo long-range orientational order but short-range translational order, similar to a hexatic phase. Our work provides guidelines to study the melting and assembly of Janus particles in two dimensions, as well as mechanisms to generate phases with specific symmetry.

DOI: 10.1103/PhysRevE.103.062607

## I. INTRODUCTION

Amphiphilic Janus particles, whose surfaces possess two opposite physical and chemical properties, have many applications in catalysis, bioimaging, and sensing [1,2]. They have both hydrophilic and hydrophobic domains on their surfaces. When their hydrophobic patches contact each other (as shown in Fig. 1), a short-range attractive potential takes place. Abundant interesting phenomena induced by anisotropy of such particles have been demonstrated, making it possible to study the nontrivial effects in a controlled manner [3–7]. In two dimensions (2D), by on-lattice simulations of close-packed Janus particles [3,8–10] people have found dimers, trimers, and rhombus chains depending on the patch size ($\theta_0 < 90^\circ$), as illustrated with our simulations in Fig. 2. In such studies, second-order phase transition for $60^\circ < \theta_0 < 90^\circ$ and continuous crossovers for $\theta_0 < 60^\circ$ between different ordered and disordered patterns were found [9,10]. Although molecular dynamics simulations with fixed density and soft potential were utilized to study melting for $60^\circ < \theta_0 < 90^\circ$ [11], 2D melting of Janus particles remains largely unexplored due to limitations of numerical methods. Mostly, 2D melting studies focus on the isotropic repulsive particle systems [12–18], and the effect of short-range attraction remains controversial [14,19–22].

In this work, with the event-chain Monte Carlo (ECMC) algorithm [23], we study the 2D melting of Janus particles by varying global area fraction $\eta$ and temperature $T$. We observe a reverse melting under cooling. Moreover, we find a pattern-dependent phase behavior. For small patch size $\theta_0 < 60^\circ$, the density boundaries of this coexistence converge at low $T$, stabilizing the reverse melting under cooling. For large patch size $\theta_0 > 90^\circ$, we find that particles can attract all six neighbors at low $T$, forming completely connected clusters, as shown in Fig. 2(d). Therefore the phase diagram is similar to the isotropic square-well particles [24–26], with an additional isostructural solid-solid transition, and finally, two coexistence regions merge into a liquid-(condensed) solid coexistence at low $T$. In other words, following reverse melting by cooling, the system finally nucleates into crystals coexisting with liquid. For the intermediate patch size $60^\circ < \theta_0 < 90^\circ$, however, the phase diagram is complicated. A critical line divides the ordered phase region on the $T \sim \eta$ diagram into two ordered phases, as a result of the formation of rhombus chains. The critical line ends by crossing the liquid-ordered coexistence boundary, leading to a reentrance of an ordered phase by further decreasing $T$ after reverse melting. The reentrant ordered phase recovers the orientational order but fails to recover the translational order, which leads to a symmetry similar to hexatic phase in isotropic particle systems.

## II. MODEL AND METHOD

### A. Kern-Frenkel model

We use the Kern-Frenkel model [27] to describe the particles, as shown in Fig. 1. In this model, particles are treated as hard spheres with diameter $\sigma$, decorated with spherical cap patches. The director $\hat{n}$ of a patch is a unit vector starting from the center of the particle pointing to the center of the patch. And the patch size $\theta_0$ is the angle between patch director and any line connecting the center of the particle and the edge of the patch. The interaction can be expressed as

$$U(\mathbf{r}_1, \mathbf{r}_2, \hat{n}_1, \hat{n}_2) = \Phi(|\mathbf{r}_{12}|) f\left(\frac{\mathbf{r}_{12}\cdot\hat{n}_1}{|\mathbf{r}_{12}|}; \theta_0\right) f\left(\frac{\mathbf{r}_{21}\cdot\hat{n}_2}{|\mathbf{r}_{21}|}; \theta_0\right), \tag{1}$$

where $\mathbf{r}_{12} = \mathbf{r}_2 - \mathbf{r}_1$, and the radial component is given by the square-well potential

$$\Phi(r) = \begin{cases} \infty & ; \quad r < \sigma \\ -\epsilon & ; \quad \sigma \leqslant r < \sigma + \delta \\ 0 & ; \quad r \geqslant \sigma + \delta. \end{cases} \tag{2}$$

*Present address: Department of Mechanical Engineering and Materials Science, Duke University, Durham, North Carolina 27708, USA.
†Corresponding author: m-olvera@northwestern.edu

 

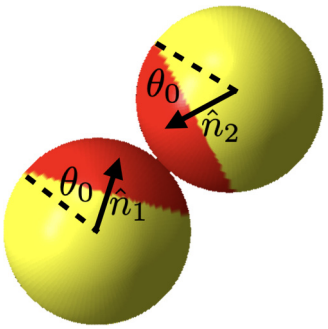


FIG. 1. Schematic illustration of Janus particle and Kern-Frenkel model.

Here $f(x;\theta_0)$ is a Heaviside step function with shift $\cos\theta_0$:

$$f(x;\theta_0) = \begin{cases} 1 & ; \quad x > \cos\theta_0 \\ 0 & ; \quad o.w. \end{cases} \tag{3}$$

In our simulations, we choose $\sigma = 2$ and $\delta = 0.04$.

### B. Method

The general dynamics of the ECMC [23] for a system with only pairwise interactions are described briefly in this section. Firstly, the Hamiltonian is divided into the following set of terms:

$$H = \sum_{i<j} \sum_{\mathcal{K}} U_{ij}^{\mathcal{K}}(\mathbf{r}_i, \mathbf{r}_j). \tag{4}$$

Here $i, j$ denote the indices of the particles, and $\mathcal{K} \in \{\mathcal{HS}, \mathcal{SW}\}$ denotes the type of interactions, where $\mathcal{HS}$ is hard sphere repulsion and $\mathcal{SW}$ is anisotropic square-well attraction, the definitions of which are in Appendix A. Each event chain starts with a randomly picked (with equal chances) particle as the first active particle. The active particle $i$ moves along the selected direction $\hat{e}$ until it collides with another particle $j$ with an interaction factor $U_{ij}^{\mathcal{K}}$. Then particle $i$ becomes inactive and stops moving, while $j$ becomes the next active particle. The event chain ends when the total displacement reaches a specified constant $l_{\text{chain}}$.

To describe this procedure, we assume the active particle moves along direction $\hat{e}$ with velocity 1. So the displacement of the active particle equals the "time" it moves, which is denoted by $\tau$. Before the collision, the position of active particle $i$ is $\mathbf{r}_i + \hat{e}\tau$, where $\mathbf{r}_i$ is the initial position of $i$. The probability that the active particle $i$ collides with particle $j$ during infinitesimal time interval $(\tau, \tau + d\tau)$ via a factor $U_{ij}^{\mathcal{K}}$ is

$$q_{ij}^{\mathcal{K}}(\tau)d\tau = \max\left\{\frac{\beta dU_{ij}^{\mathcal{K}}(\mathbf{r}_i + \hat{e}\tau, \mathbf{r}_j)}{d\tau}, 0\right\}d\tau, \tag{5}$$

where $\beta = 1/k_BT$, $k_B$ is the Boltzmann constant, and $T$ is the temperature. The collisions by different factors happen independently. Therefore, in the computer simulation, we generate random variables representing the collision time $\tau_{ij}^{\mathcal{K}}$ for each factor $U_{ij}^{\mathcal{K}}$ associated with the active particle $i$. And we select minimum $\tau_{ij}^{\mathcal{K}}$ over all $j$ and $\mathcal{K}$ as the next event time $\tau_i$. The active particle $i$ jumps directly by $\tau_i$, stops moving, and then activates corresponding $j$ as the next moving particle. For an interaction $U_{ij}^{\mathcal{K}}(\mathbf{r}_i, \mathbf{r}_j)$, the event time $\tau_{ij}^{\mathcal{K}}$ is subject to the following distribution:

$$\pi_{ij}^{\mathcal{K}}(\tau) = \exp\left(-Q_{ij}^{\mathcal{K}}(\tau)\right)q_{ij}^{\mathcal{K}}(\tau), \tag{6}$$

where $Q_{ij}^{\mathcal{K}}(\tau) = \int_0^\tau q_{ij}^{\mathcal{K}}(s)ds$. To generate $\tau_{ij}^{\mathcal{K}}$, we need to use the cumulative distribution function

$$F_{ij}^{\mathcal{K}}(\tau) = \int_0^\tau \pi_{ij}^{\mathcal{K}}(\xi)d\xi = 1 - \exp\left(-Q_{ij}^{\mathcal{K}}(\tau)\right). \tag{7}$$

If we treat $F_{ij}^{\mathcal{K}}(\tau)$ as a function of a random variable $\tau$, $1 - F_{ij}^{\mathcal{K}}(\tau)$ will be also a random variable that is uniformly distributed in the interval (0,1]. So we need to generate a random variable $r \in (0, 1]$ and solve the equation

$$Q_{ij}^{\mathcal{K}}(\tau) = -\ln r \tag{8}$$

to get $\tau_{ij}^{\mathcal{K}}$. For each type of interaction, generating methods of $\tau_{ij}^{\mathcal{K}}$ can be found in Appendix A. In each loop, the moving directions $\hat{e}$ are selected along $+x, +y, -x, -y$, sequentially, with $l_{\text{chain}} = L/2$, where $L$ is the size of the system in the moving dimension.

The rotational degrees of freedom are updated in each loop following the Metropolis Monte Carlo scheme. The directors for two neighboring particles are decoupled in the pairwise interaction. Therefore when we update the directors, the interaction behaves like a one-body potential. The most convenient way to update these directors is the traditional Metropolis Monte Carlo. That is, for a chosen particle $i$, a new patch director $\hat{n}_i'$ is proposed first with uniform distribution on the unit sphere, and we compute the energy change $\Delta E_i(\hat{n}_i \to \hat{n}_i')$ due to this rotation and accept this rotation with probability $\min\{1, \exp(-\beta\Delta E_i)\}$. Here the computation of $\Delta E_i$ can be performed by only summing over the interactions with neighboring particles of particle $i$. Due to the short-range property of the interactions, this updating can be performed in parallel by taking advantage of the cell list provided in our ECMC code, as well as the check-board updating scheme [28]. We used OPENMP to implement this update.

## III. RESULTS AND DISCUSSION

### A. The equation of state and the heat capacity

Large-scale simulations with $512^2 = 262\,144$ particles were performed. The pressure $P$ can be calculated in a very simple and precise way [23]:

$$\beta P = \frac{4\eta}{\pi\sigma^2}\left[1 + \left\langle \frac{1}{l_{\text{chain}}} \sum_{\textbf{eventsinchain}} \mathbf{r}_{ij} \cdot \hat{e} \right\rangle_{\text{chain}}\right], \tag{9}$$

where $\eta = \frac{N\pi\sigma^2}{4A}$ is the area fraction of the whole system, and $\mathbf{r}_{ij}$ is the position difference between the target particle $j$ and the active particle $i$ at the event. The summation is over all the events in one event chain, and the bracket is the average over all the event chains. The instant $P$ value defined in Eq. (9) and potential energy $E$ value are monitored to ensure equilibrium.

The equation of state (EOS) curves $P(\eta)$ for $\theta_0 = 58^\circ$ ($\theta_0 < 60^\circ$), $\theta_0 = 80^\circ$ ($60^\circ < \theta_0 < 90^\circ$), $\theta_0 = 100^\circ$ ($\theta_0 > 90^\circ$), and isotropic particles ($\theta_0 = 180^\circ$) are plotted in Fig. 3.

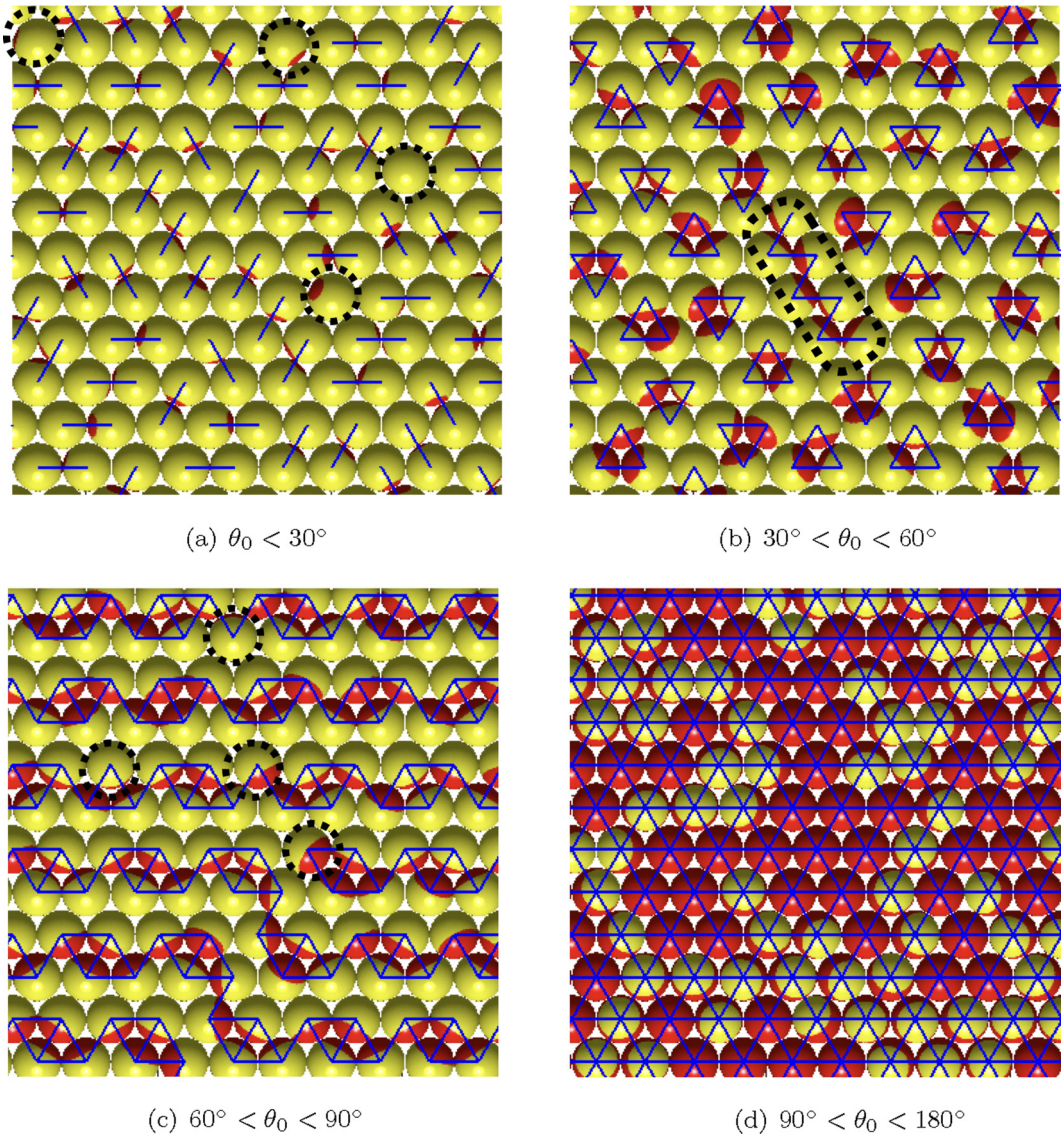

(a) $\theta_0 < 30°$ (b) $30° < \theta_0 < 60°$

(c) $60° < \theta_0 < 90°$ (d) $90° < \theta_0 < 180°$

FIG. 2. Ground states at close-packed regime. Solid lines are bonds connecting two neighboring particles if their patches attract each other. The defects are marked by dotted curves. (a) $\theta_0 < 30°$, dimers. Defects are isolated particles, which do not attract any particle. (b) $30° < \theta_0 < 60°$, trimers. Defects are mainly single-strained chains. (c) $60° < \theta_0 < 90°$, rhombus chains. Defects are the ends of chains and imperfect rhombus. (d) $\theta_0 > 90°$, completely connected clusters.

Plateaus are seen in these curves, which are clear characteristics of the Mayer-Wood loop [29] of a first-order transition. For $\theta_0 > 90°$ [Figs. 3(c) and 3(d)], the metastable states in the simulations cause multiple pressure values at the same total area fraction value $\eta$, depending on the initial configuration. We can see two plateaus at low temperatures, where the first ones (low $\eta$) are the liquid-ordered phase transitions and the second ones (high $\eta$) are the solid-solid transitions. At sufficiently low $T$, $P$ becomes flat at a wide region, corresponding to liquid-condensed solid coexistence. By checking the EOS and snapshots directly (representative snapshots are shown in Figs. 9 and 10), we are able to determine the boundaries of the different phases. Figures 3(e) and 3(f) show the enlarged plot of the pressure $P$ versus $\eta^{-1} = A/(NA_0)$ curves for $T = \varepsilon/(5k_B)$ and $T = \varepsilon/(8k_B)$, respectively, for different system sizes $N$. As depicted in these figures, the curves are not monotonic. Theoretically, the peak and the valley in the Mayer-Wood region get sharper as the system size $N$ gets smaller, which is an effect of interfacial energy [17,18]. However, in our simulations the difference between various $N$ is not detectable due to statistical fluctuations: This demonstrates that $N$ is sufficiently large in order to exclude the finite-size effect in this first-order transition. The $T \to \infty$ case is shown as blue dotted curves in all the figures as a reference, which has a flat region between $\eta_0 = 0.7$ and $\eta_1 = 0.718$, identical to the result of hard disks [17], verifying our code.

The constant volume heat capacities are computed in the following way:

$$C_V = k_B\beta^2[\langle E^2\rangle - \langle E\rangle^2]. \tag{10}$$

The constant volume heat capacity per particle with respect to temperature, $C_V(T)/(k_BN)$, shows a smooth peak in the ordered phase for $\theta_0 = 58°$ [$\theta_0 < 60°$, see Fig. 4(a)],

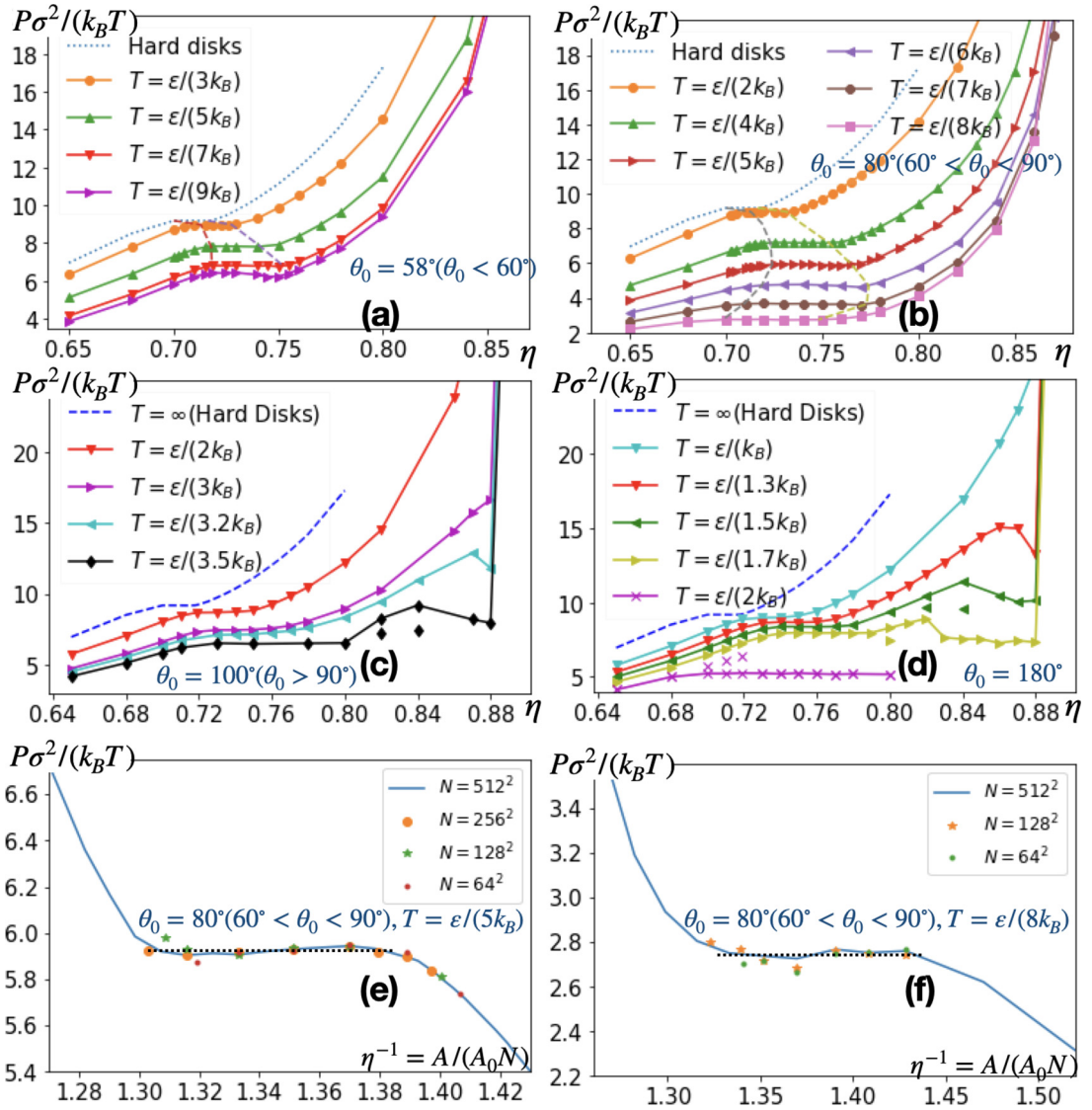


FIG. 3. Equation of state $P(\eta)$ for (a) $\theta_0 = 58°$ ($\theta_0 < 60°$), (b) $\theta_0 = 80°(60° < \theta_0 < 90°)$, (c) $\theta_0 = 100°(\theta_0 > 90°)$, and (d) isotropic particles $\theta_0 = 180°$. For (a), (b), dashed lines connect lower (upper) boundaries of coexistence. For (c), (d) the off-curve points with the same symbols are the values measured in the simulation with different initial configurations. Multiple values at the same densities are caused by hysteresis. (e), (f) Enlarged equation of state $P(\eta^{-1})$ at different system sizes for $\theta = 80°$ at (e) $T = \varepsilon/(5k_B)$ and (f) $T = \varepsilon/(8k_B)$ [corresponding to two curves in (b)].

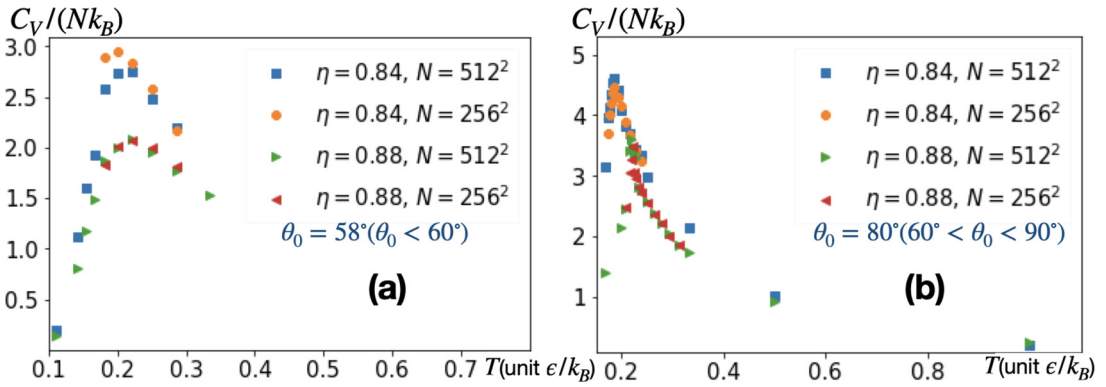


FIG. 4. Constant volume heat capacities (per volume) $C_V(T)/(k_BN)$ for (a) $\theta_0 = 58°$ and (b) $\theta_0 = 80°$ at different area fractions $\eta$ and system sizes $N$.

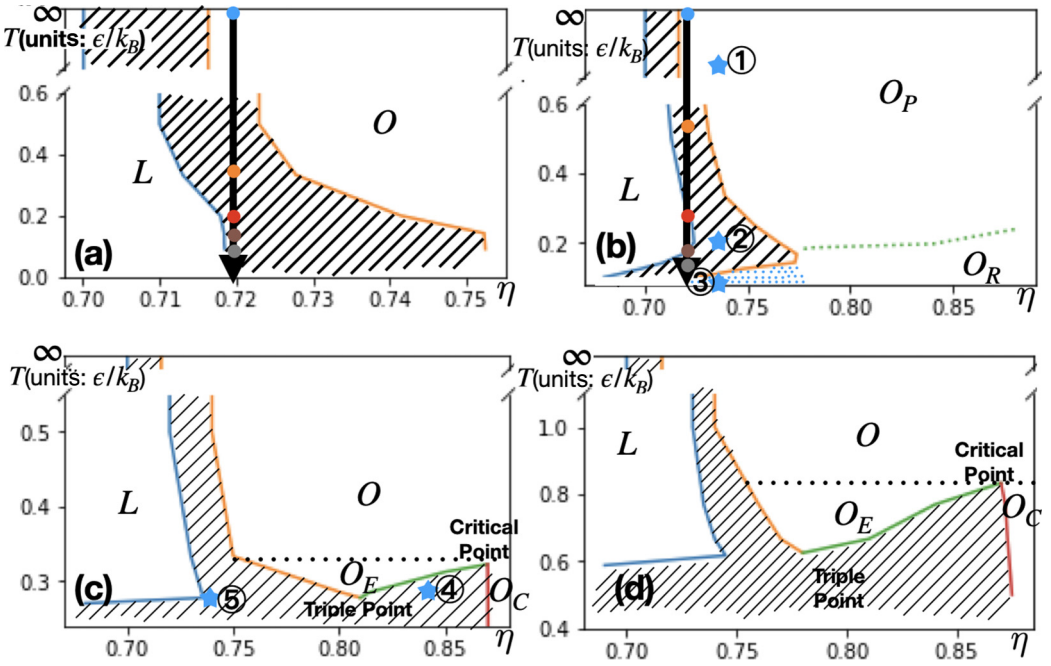


FIG. 5. Phase diagrams for (a) $\theta_0 = 58°$, (b) $\theta_0 = 80°$ (c) $\theta_0 = 100°$, and (d) isotropic particles ($\theta_0 = 180°$). The shadow zones represent coexistence. The green dotted curve in (b) is a critical line. In the blue dotted zone, short-range translational order and (pseudo) long-range orientational order are observed. For (c), (d), the critical points and triple points are labeled. The $y$ axis is broken to show the condition of $T = \infty$. The solid arrows in (a) and (b), together with the colored dots on them, represent the annealing process in Fig. 11. The blue stars represent systems in the snapshots in this article: ① Fig. 6(a), ② Fig. 7, ③ Fig. 6(b), ④ Fig. 9, and ⑤ Fig. 10.

indicating no phase transition in the dense region. On the other hand, sharp peaks are observed in the ordered phase region for $\theta_0 = 80°$ [$60° < \theta_0 < 90°$, see Fig. 4(b)], and the peaks get sharper as the system size increases, strongly indicating second-order phase transitions. We also measure the $C_V$ curve for the case $\eta = 0.78$ and $\theta_0 = 80°$. This curve has big statistical fluctuations due to insufficient sampling and is close to the curve of $\eta = 0.84$ in Fig. 4 (see Appendix D).

### B. Phase diagram

With the aforementioned analyses, we obtain the phase diagrams as shown in Fig. 5. The blue solid curve indicates the upper bound of a pure liquid phase, denoted by $L$, and the yellow solid curve indicates the lower bound of a pure ordered phase, denoted by $O$. Here $O$ may include subphases which possess different symmetries or orders. The shadow region between these two curves denotes the $L - O$ coexistence region.

For case (a) $\theta_0 < 60°$, as shown in Fig. 5(a), the $L - O$ coexistence region converges to a constant value as $T$ decreases. This stability is due to the fact that clusters induced by attractions reach a constant size when $T \to 0$ (see Appendix C for cluster size analysis). These clusters are mainly dimers ($\theta_0 < 30°$, and cluster size is 2) or trimers ($30° < \theta_0 < 60°$, and cluster size is 3), with some thermal excited single-strained chains [Figs. 2(a) and 2(b)]. As $T \to 0$, the single-strained chains will disappear since they have higher energies. Therefore the compression process of the system at extremely low $T$ is equivalent to compressing hard dimers/trimers, leading to converged $P(\eta)$ curve at low $T$.

In contrast, for $\theta_0 > 60°$, the $L - O$ coexistence boundaries diverge as $T \to 0$ due to the fact that the clusters grow rapidly as $T \to 0$ (for definition of cluster size, see Appendix C). Specifically, for case (b) $60° < \theta_0 < 90°$ [Fig. 5(b)], the $O$ phase is divided into two subphases by a critical line (the green dotted curve): The plastic ordered phase $O_P$ with disordered patch directions [Fig. 6(a)] and $O_R$ phase, where patch directions are ordered and assemble into long clusters, that is, the rhombus chains [see Fig. 6(b)]. This critical line ends by crossing the $L - O$ coexistence upper boundary at $\eta'(\approx 0.78)$ and $T'(\approx 0.179\epsilon/k_B)$. Below $T'$ the two $L - O$ coexistence boundaries shift to lower $\eta$ values quickly, indicating that pure $O_R$ phase can go to rather low densities at very low $T$. On the critical line, the critical temperature increases monotonically with $\eta$. At the highest total area fraction we measured, $\eta = 0.88$, the critical temperature is about $0.22\epsilon/k_B$, consistent with the result of on-lattice simulations of close-packed systems ($\eta = 0.91$, $T \approx 0.26\epsilon/k_B$) in trends [9]. In Figs. 6 and 7, we list different snapshots for global area fraction $\eta = 0.73$ at different temperatures. For Fig. 6(a) the system is at high temperature ($T = \epsilon/k_B$, corresponding to star ① in Fig. 5), whereas for Fig. 6(b) it is at low temperature ($T = \epsilon/12k_B$, corresponding to star ③ in Fig. 5). These two systems are ordered phases with different orders and symmetries, which is explained in Sec. III D. For Fig. 7, the system is at an intermediate temperature ($T = \epsilon/5k_B$, corresponding to star ② in Fig. 5), which is a coexistence between $L$ phase and $O_P$ phase (or its premelting hexatic phase). Figure 8 shows snapshots of Fig. 7 at different loops when the system is close to the equilibrium state, where two phases approach a well-separated state.

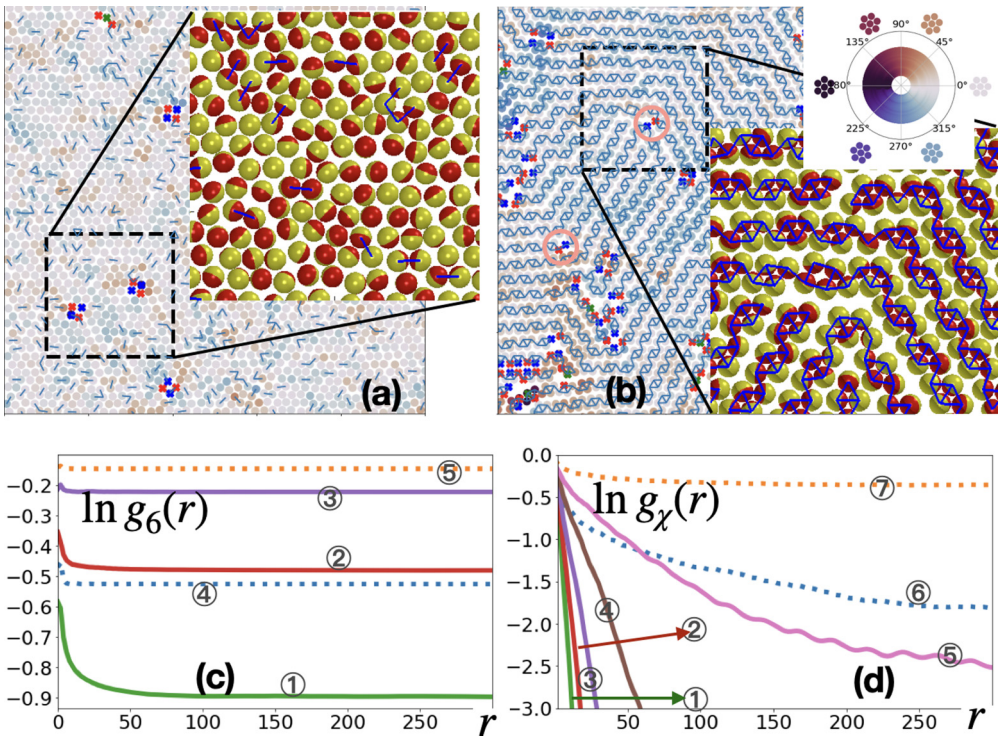


FIG. 6. Snapshot at area fraction $\eta = 0.73$. (a) An $O_P$ phase ($T = \epsilon/k_B$, corresponding to the star ① in Fig. 5). (b) An $O_R$ phase ($T = \epsilon/12k_B$, corresponding to the star ③ in Fig. 5). In the big pictures, blue, red, and green dots are seven-, five-, and eightfold disclinations, respectively. For other particles, colors represent orientation of $\psi_6$, as shown in the color wheel. Blue lines represent the attractive interactions. Circles mark isolated dislocations. The insets are details of the dashed windows. (c) Orientational correlation functions $g_6$ in log scale. Solid curves are $O_R$ phase at $T = \epsilon/(12k_B)$, ① $\eta = 0.72$, ② $\eta = 0.76$, ③ $\eta = 0.8$, and dotted curves are $O_P$ phase at $T = \epsilon/k_B$, ④ $\eta = 0.73$, ⑤ $\eta = 0.8$. (d) Translational correlation functions $g_\chi(r)$ in log scale. Solid curves are $O_R$ phase at $T = \epsilon/(12k_B)$, ① $\eta = 0.72$, ② $\eta = 0.74$, ③ $\eta = 0.76$, ④ $\eta = 0.78$, ⑤ $\eta = 0.8$, and dotted curves are $O_P$ phase at $T = \epsilon/k_B$, ⑥ $\eta = 0.73$, ⑦ $\eta = 0.8$.

For case (c) $\theta_0 > 90°$ [Figs. 5(c) and 5(d)], apart from the $L - O$ transitions bounded by blue and yellow solid lines, there is another coexistence region, bounded by green and red solid lines, between the expanded solid phase $O_E$ and condensed solid phase $O_C$. The difference between $O_E$ and $O_C$ is that in $O_C$ most particles attract six neighbors, whereas in $O_E$ they cannot (see Fig. 9, which corresponds to star ④ in Fig. 5). As a result, $O_C$ is more compact. This solid-solid transition has been predicted specifically for isotropic particles [$\theta_0 = 180°$, see Fig. 5(d)] in Refs. [24,25]. Below the critical temperature $T_c$ and above the triple point temperature $T_3$, the solid phase $O$ is split into $O_E$ and $O_C$. For $T < T_3$, two coexistence regions merge into one and become a coexistence between liquid $L$ and condense solid $O_C$, preempting $O_E$, and the upper density bound of liquid phase drops downwards quickly (see Fig. 10, which corresponds to star ⑤ in Fig. 5).

### C. Reverse melting

In the phase diagrams, the $L - O$ coexistence (or $L - O_P$, $L - O_E$, for different $\theta_0$) boundaries shift toward higher $\eta$ as $T$ decreases from very high $T$. This means that if we cool a solid system at some specific density (e.g., $\eta = 0.72$) with constant volume restriction, it melts or partially melts. This counterintuitive reverse-melting behavior observed here is qualitatively in agreement with the prediction in Refs. [24,25], where small-scale simulations were performed for isotropic particles. Since this trend starts continuously from pure hard disks systems ($T \to \infty$), we can infer that it is an effect of the competition between entropy and short-range attractions. At very high $T$, the attractive interaction is negligible, so the rigid repulsion dominates, resulting in entropy-driven crystallization where particles are not necessarily compact. For example, at area fraction $\eta^* = 0.72$, the average distance between particles is $d^* \approx 1.12\sigma > \sigma + \delta$, even though it is already a solid phase. As $T$ decreases from a very high value, particles get closer to attract each other to lower the energy. To compensate the total area constraint, the system breaks into small compact domains (with $\sim 10^2$ particles) by forming percolated disclination networks, which are called grain boundaries [16]. Each domain has a homogeneous $\psi_6$ orientation, as shown in Fig. 7(c). Here $\psi_6$ is defined as

$$\psi_6^k = \frac{1}{N_k} \sum_{l=1}^{N_k} \exp(6i\phi_{kl}) \tag{11}$$

for particle $k$, with the average over all the neighbors of particle $l$, and $\phi_{kl}$ is the angle between a reference direction and the bond connecting $k$ and $l$, $N_k$ is the number of neighboring particles, and neighboring relation is built by Voronoi construction. In Fig. 8 we list the snapshots of a coexistence system at different simulation steps. In the first column it is shown that the coexistence boundaries are flexible. In the second column it is shown that the grain boundaries are flexible and evolving rapidly during the simulation. In the third

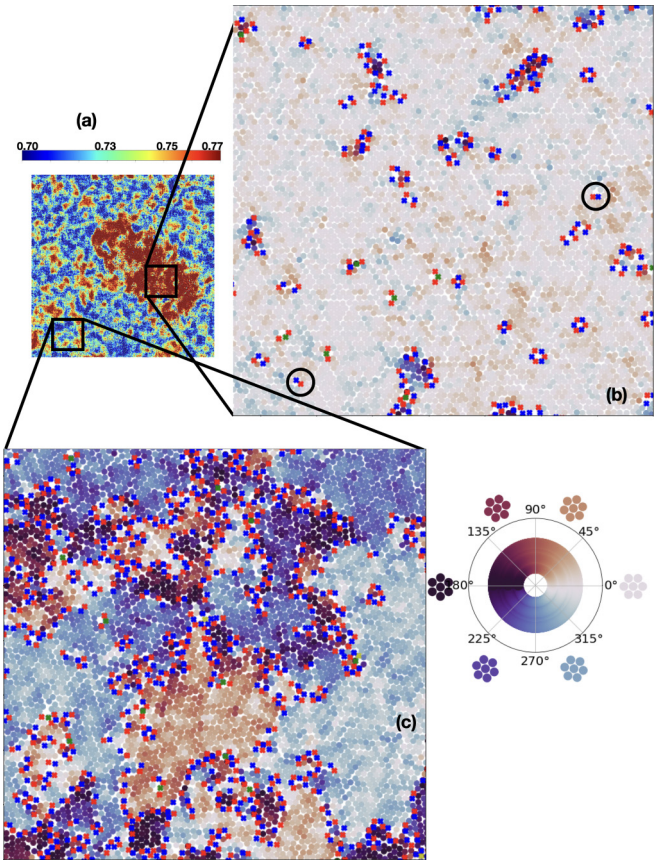


FIG. 7. Snapshot of a coexistence for $\theta_0 = 80^\circ$, at $T = \epsilon/(5k_B)$, with global area fraction $\eta = 0.73$. This figure corresponds to the star ② in Fig. 5. (a) Coarse-grained local $\eta(\mathbf{x})$ colors map. The liquid phase ($L$) with local $\eta \approx 0.725$ coexists with an ordered phase with local $\eta \approx 0.775$. (b) Enlarged snapshot of ordered phase $O_P$. Blue and red dots are the seven- and fivefold disclinations. The colors of other particles are the orientation of $\psi_6$. Circles mark isolated dislocations. (c) Enlarged snapshot of liquid phase $L$.

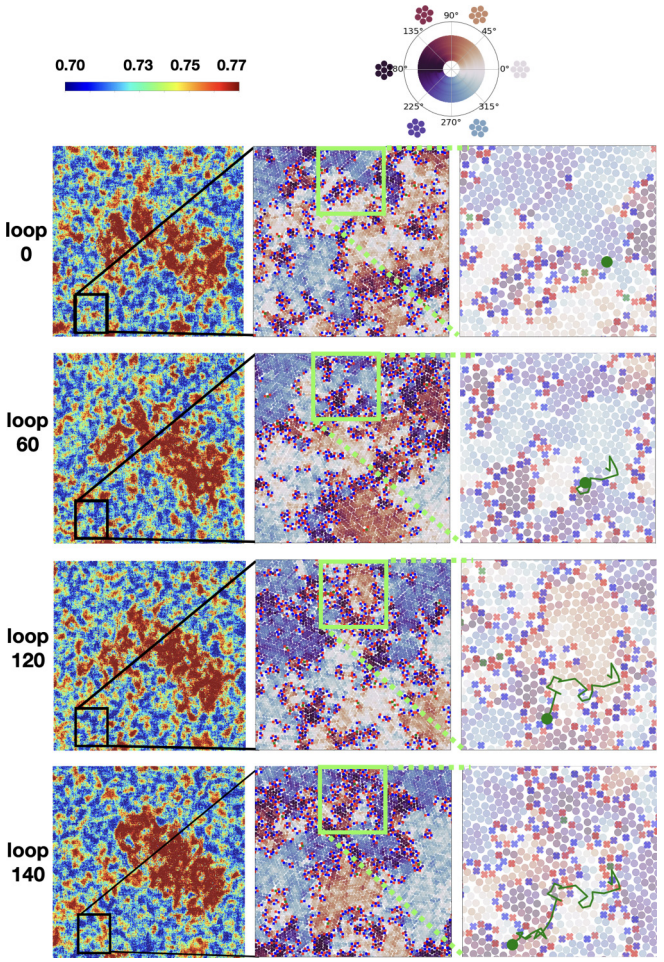


FIG. 8. Snapshots of coexistence between liquid $L$ (blue) phase and ordered $O_P$ (red) phases at different simulation steps. Here $\theta_0 = 80^\circ$, at $T = \epsilon/(5k_B)$, and global area fraction is $\eta = 0.73$. This figure shows the same system with Fig. 7. First column: Coarse-grained local $\eta(\mathbf{x})$ colors map. Second column: Enlarged snapshot of liquid phase $L$ in the black windows in the first column. Third column: Enlarged snapshots of green windows in the second column. In the third column, we mark a selected particle with a big green dot in each snapshot. The trace of this particle is draw as green solid curve. The "loop 0" is selected after sufficient long MC simulation when the system gets close to equilibrium.

column it is shown that the particles are moving instead of oscillating around their equilibrium position. The flexibility of grain boundaries and coexistence boundaries, as well as the diffusion of particles, suggest that the melt phase is not a polycrystal.

In Fig. 11 we show structure factor maps $S(\mathbf{q})$ with $\eta^* = 0.72$ at different $T$ for $\theta_0 = 58^\circ$ and $\theta_0 = 80^\circ$, respectively. The positions of these systems in the phase diagram (Fig. 5 (a-b)) are marked by different colored dots along the solid arrows. We can see that, for both cases, the $S(\mathbf{q})$ maps gradually lose their sixfold symmetry by cooling from high $T$, as a result of reverse melting. Specifically, for $\theta_0 = 58^\circ$, the loss of sixfold symmetry is stable with $T$ decreases. However, a nontrivial phase behavior was observed for $\theta_0 = 80^\circ$, i.e., the sixfold symmetry is recovered eventually, indicating a reentrance of ordered phase ($O_R$), as a result of the formation of long rhombus chains at low $T$.

### D. The reentrant $O_R$ phase and its loss of translational order

As mentioned in the previous section, for $60^\circ < \theta < 90^\circ$, the system finally recovers the sixfold symmetry, which corresponds to a reentrance to $O_R$ phase. For such reentrant $O_R$ phases, we observed a large number of isolated dislocations [see Fig. 6(b)], which indicates loss of translational order. Here, a dislocation is defined as a pair of fivefold and sevenfold nearest neighbor disclinations [13,14]. The translational order parameter $\chi$ is defined as

$$\chi_k = \exp(i\mathbf{q}_0 \cdot \mathbf{x}_k) \tag{12}$$

on particle $k$, with first Bragg peaks $\mathbf{q}_0$. The value of $\mathbf{q}_0$ is determined by finding the $\mathbf{q}$ value with maximum $S(\mathbf{q})$ numerically. In Fig. 6(d), the correlation functions of $\chi$, $g_\chi$, decay exponentially at low $T = \epsilon/12k_B$ in $0.72 \leqslant \eta \leqslant 0.78$, whereas for high $T = \epsilon/k_B$, it decays with power law. The result shows that for such systems, the translational order is

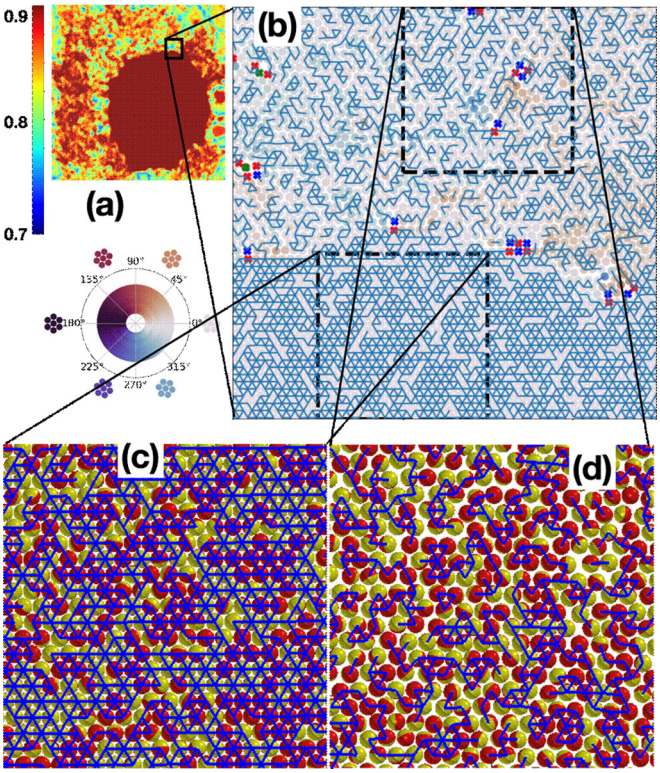


FIG. 9. Isostructural solid-solid transition of system with $\theta_0 = 100^\circ$, $T = \epsilon/(3.4k_B)$, and global area fraction $\eta = 0.84$. This figure corresponds to star ④ in Fig. 5. (a) Density profile. Colors represent density. (b) $\psi_6$ maps of the enlarged two-phase interface. Colors of particles are the orientation of $\psi_6$, which are explained in the color wheel. Blue, red, and green dots are seven-, five-, and eightfold disclinations, respectively. Blue lines correspond to bonds, which represent the attractive interactions. We can see that both the expanded $O_E$ phase and dense $O_C$ phase share the same sixfold hexagonal structure but with different densities and different bond connectivities. The density difference comes from the strength of the attractive connection. (c), (d) Enlarged snapshots of $O_C$ and $O_E$ phases, respectively. The details of patched particles are shown.

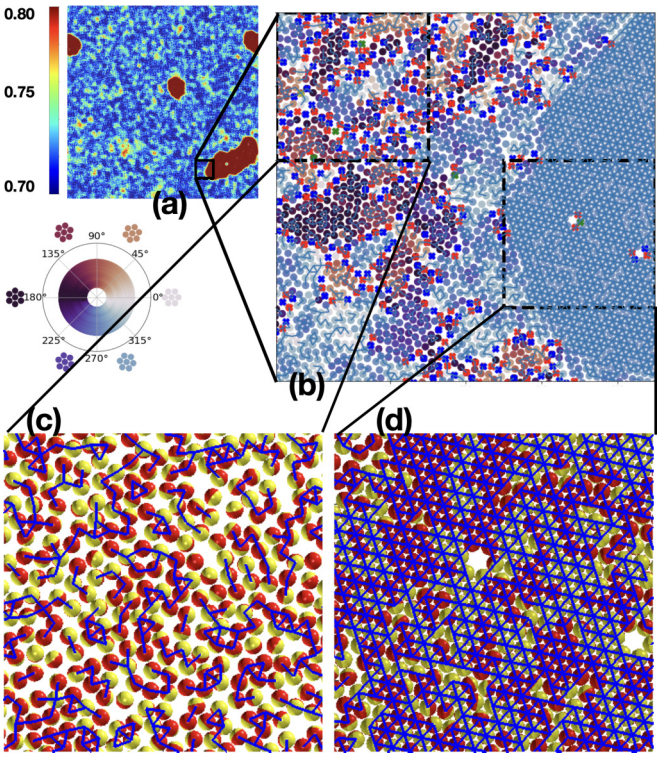


FIG. 10. Liquid-condensed solid ($L$-$O_C$) coexistence of system with $\theta_0 = 100^\circ$, $T = \epsilon/(3.5k_B)$, $\eta = 0.73$. This figure corresponds to star ⑤ in Fig. 5. (a) Density profile. Colors represent density. (b) $\psi_6$ maps of the enlarged two-phase interface. Colors of particles are the orientation of $\psi_6$, which are explained in the color wheel. Blue, red, and green dots are seven-, five-, and eightfold disclinations, respectively. Blue lines are bonds which represent the attractive interactions. (c), (d) Enlarged snapshots of $L$ and $O_C$ phases, respectively. The details of patched particles are shown. At sufficient low $T$, the phase transition of systems with $\theta_0 > 90^\circ$ is between liquid and condensed solid $O_C$ phase directly. The defects of $O_C$ are vacancies, and no free dislocations are observed.

lost by cooling, even though the orientational order $\psi_6$ is recovered, as shown in Fig. 6(c).

This reverse order-disorder transition by cooling can be explained by the formation of rhombus chains. The rhombus chains compact particles along their longitudinal direction and grow either along their original directions or turn $\pm 60^\circ$ from their original directions [see Fig. 12(a) and Fig. 12(b)]. This selectivity of growing direction promotes sixfold rotational symmetry even at low $\eta$, resulting in reentrance to the ordered phase $O_R$, with (pseudo) long-range orientational order $\psi_6$. On the other hand, the loose alignments and flexibility of rhombus chains [see Fig. 12(c)] generate more dislocations [see Fig. 6(b)], breaking the transitional order $\chi$ of the $O_R$ phase at low $\eta$. The flexibilities are supported by the bending of the rhombus chains at the expense of energy or entropy. Bending within $2\theta_0 - 120^\circ$ does not change the energy, but such bending is entropically unfavorable, since it restricts the solid angle of pivot particle's free rotation. In this case, strong attraction leads to the loss of translational order, in contrast to other attractive systems where strong attraction promotes the long-range order.

In Fig. 5(b), the subregion of $O_R$ where systems have short-range translational order is marked with blue dots. If systems are compressed (at constant temperature) to the close-packed regime, the translational order recovers. In Fig. 6(d) this trend is shown. At $T = \varepsilon/(12k_B)$ and $\eta = 0.8$, $g_\chi$ decays in power law, in contrast with the lower density case ($\eta < 0.78$) where $g_\chi$ decays exponentially. It is unclear within our simulation whether or not this change of order is a phase transition.

Systems of isotropic particles can have a hexatic phase, with no translational order $\chi$ while keeping orientational order $\psi_6$. The hexatic phase is accompanied by the emergence of isolated dislocations. In the $O$ phase region of $L - O$ coexistences [except for $L - O_R$ coexistence, see Fig. 7(b)], as well as the $O_E$ region of $O_E - O_C$ coexistences for $\theta_0 > 90^\circ$ [see Fig. 9(b)], isolated dislocations are always observed. Since such dislocations are at low density, it requires larger-scale simulations to verify the possibility of a hexatic phase before the first-order transition to liquid $L$ or condensed solid $O_C$.

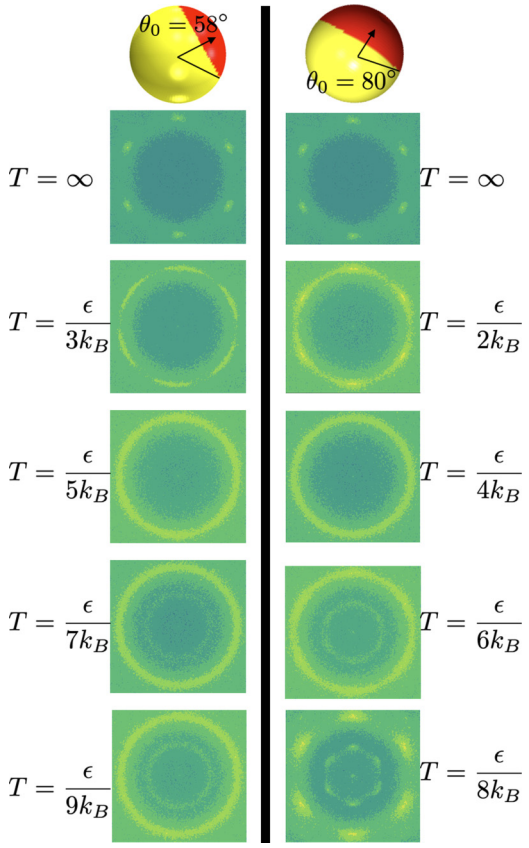


FIG. 11. Structural factor maps $S(\mathbf{q})$ for $\theta_0 = 58°$(up) and $\theta_0 = 80°$(down) at $\eta = 0.72$ and different $T$. These systems correspond to different colored dots along the solid arrows in Fig. 5.

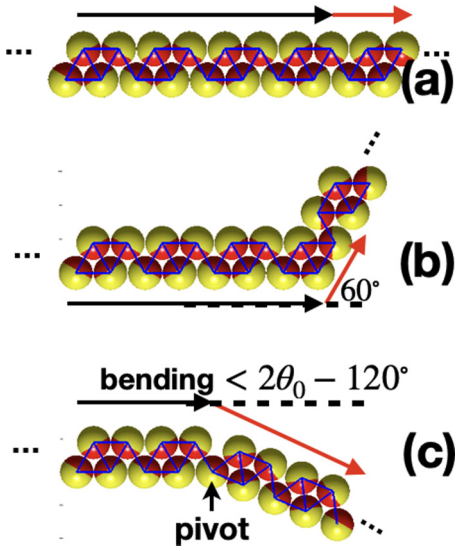


FIG. 12. Schematic illustration of growing direction of rhombus chains. The black lines are original directions, the red lines are new growing directions. (a) the chain grows along the original direction, (b) the chain turns 60 degrees from the original direction, (c) the chain bends from the original direction, with the pivot particle marked.

## IV. CONCLUSION

In conclusion, rich types of transitions are found with a simple Kern-Frenkel model and the hybrid ECMC. Moreover, reverse order-disorder transitions are identified, including a reverse melting for all patch sizes, and a reverse translational order loss for $60° < \theta_0 < 90°$. The results can be experimentally verified using narrow-disperse attractive Janus colloids when particles are rigid and the attractions are short and sensitive to temperature. Our study provides a better understanding of the phase behavior of such Janus particle systems and offers guidelines in experimental design to achieve certain thermal and electrical transport properties and for applications such as tunable optical sensing devices.

## ACKNOWLEDGMENTS

We thank Dr. Wei Li for helpful discussions, as well as Dingwen Qian for his contribution to the C++ code. This work was supported by the Center for Bio-Inspired Energy Science, an Energy Frontier Research Center funded by the US Department of Energy (DOE) Office of Basic Energy Sciences under Award No. DE-SC0000989.

## APPENDIX A: EVENT TIME COMPUTATION

For simplicity, we divide the Kern-Frenkel interaction $U$ into two parts: Hard sphere interactions $U^{\mathcal{HS}}$ and directional square-well interaction $U^{\mathcal{SW}}$, i.e., $U = U^{\mathcal{HS}} + U^{\mathcal{SW}}$. The hard sphere interactions $U^{\mathcal{HS}}$ can be written as

$$U^{\mathcal{HS}}(r) = \begin{cases} \infty & ; \quad r < \sigma \\ 0 & ; \quad r \geqslant \sigma \end{cases} \tag{A1}$$

and directional square-well interaction $U^{\mathcal{SW}}$ is

$$U^{\mathcal{SW}}(\mathbf{r}_1, \mathbf{r}_2, \hat{n}_1, \hat{n}_2) = \Theta(|\mathbf{r}_{12}|) f\left(\frac{\mathbf{r}_{12} \cdot \hat{n}_1}{|\mathbf{r}_{12}|}; \theta_0\right) f\left(\frac{\mathbf{r}_{21} \cdot \hat{n}_2}{|\mathbf{r}_{21}|}; \theta_0\right), \tag{A2}$$

where

$$\Theta(r) = \begin{cases} -\epsilon & ; \quad r < \sigma + \delta \\ 0 & ; \quad r \geqslant \sigma + \delta. \end{cases} \tag{A3}$$

We treat them as different factors in the ECMC, meaning that $U^{\mathcal{HS}}$ and $U^{\mathcal{SW}}$ generate collision events independently. Since these two terms do not cancel each other, this decomposition does not change the total event rate; therefore the performance would be the same as the merged factor implementation.

### 1. Event time of hard spheres

For hard sphere interaction $U^{\mathcal{HS}}$, it is easy to implement its event-time generator. Suppose particle 1 is moving along the $x$ axis. The shortest distance between particle 1 and particle 2 is $d = \sqrt{\Delta y^2 + \Delta z^2}$. Here, $\Delta y = y_2 - y_1$ and $\Delta z = z_2 - z_1$. Note that we need to wrap $\Delta y$ within $[-L_y/2, L_y/2]$ and so as $\Delta z$. Before computing the event time, we wrap $\Delta x = x_2 - x_1$ into $(0, L_x)$. We limit the legal event time to be less than $L_x$.

(1) If $d > \sigma$, collision will not happen, and the program returns a big value (like $2L_x$) as the event time.

(2) If $d < \sigma$, the event time is determined as $\Delta x - \sqrt{\sigma^2 - d^2}$. Note that the result is deterministic. The reason for this deterministic event time is because the potential is either 0 or $\infty$, and the solution of Eq. (8) is always at the position where particles start to contact each other.

#### 2. Event time of directional square-well potential

The event-time generator for directional square-well potential $U^{\mathcal{SW}}$ is shown in the following. We can obtain

(1) Time interval where particle 1 is attracted to particle 2 by isotropic square well:

$$I^{\mathcal{SW}} = [\Delta x - \sqrt{(\sigma+\delta)^2 - d^2}, \Delta x + \sqrt{(\sigma+\delta)^2 - d^2}]. \tag{A4}$$

Here $\Delta = x_2 - x_1$ and we do not wrap it first, but when we compute $d$, $\Delta y$ and $\Delta z$ are wrapped, $\Delta y \in [-L_y/2, L_y/2]$ and $\Delta z \in [-L_z/2, L_z/2]$.

(2) Time interval $I^1$ where angle $\langle \hat{n}_1, dr \rangle$ is smaller than $\theta_0$. This interval can be obtained by solving the inequality $\frac{(\mathbf{r}_{12} - s\hat{n})\cdot\hat{n}_1}{|\mathbf{r}_{12} - \hat{n}s|} \geqslant \cos\theta_0$, which can be reduced to a one-variable quadratic inequality of $s$. Note that when computing this interval, we do not consider the periodic images in the $x$ axis.

(3) Time interval $I^2$ where the angle $\langle \hat{n}_2, dr \rangle$ is smaller than $\theta_0$. This can be also obtained similarly as described in 2.

Then we can define $I = I^{\mathcal{SW}} \cap I^1 \cap I^2$, which is the attractive region. Here, $I$ is composed of many disjoint intervals $I = [s_1, s_1^*] \cup [s_2, s_2^*] \cdots \cup [s_n, s_n^*]$. In these intervals, the upper bound is wrapped within $[0, L_x]$. That is, if $s_i^* > L_x$, make $s_i \leftarrow s_i - L_x$ and $s_i^* \leftarrow s_i^* - L_x$; if $s_i^* < 0$, make $s_i \leftarrow s_i + L_x$ and $s_i^* \leftarrow s_i^* + L_x$. Then we sort them according to the value of $s_i^*$ in ascending order. Next, we generate a random variable $r$ and compute $\epsilon^* = -\ln(r)$.

(1) If $\epsilon^* > n\epsilon$ or $I = \emptyset$, particles 1 and 2 will not collide within the time window $[0, L_x]$, so the program returns a big value (such as $2L_x$).

(2) Or else, if $(n-1)\epsilon < \epsilon^* < n\epsilon$, the program returns $s_n^*$.

Implementation in our C++ code has been optimized for such a generator.

## APPENDIX B: PRESSURE COMPUTATION

The pressure is computed based on the virial theorem [23]:

$$\beta P = \frac{4\eta}{\pi\sigma^2}\left[1 - \frac{\beta}{4N}\sum_i \sum_{j:j\neq i} \langle \mathbf{r}_{ij} \cdot \mathbf{F}_{ij} \rangle\right], \tag{B1}$$

where $\mathbf{r}_{ij} = \mathbf{r}_j - \mathbf{r}_i$, $\mathbf{F}_{ij} = -\nabla_{\mathbf{r}_{ij}} U(\mathbf{r}_{ij}, \hat{n}_i, \hat{n}_j)$, and $\langle ... \rangle$ is the ensemble average. $\eta$ is the area fraction of hard spheres, $\beta = 1/(k_B T)$, and $N$ is the number of particles. Obviously, $\mathbf{F}_{ij} = -\mathbf{F}_{ji}$. For isotropic systems, $\langle \mathbf{r}_{ij} \cdot \mathbf{F}_{ij} \rangle = \langle x_{ij} F_{ij}^x \rangle + \langle y_{ij} F_{ij}^y \rangle = 2\langle (\mathbf{r}_{ij} \cdot \hat{e})(\mathbf{F}_{ij} \cdot \hat{e}) \rangle$, where $\hat{e}$ is a unit vector in an arbitrary direction. So we can rewrite Eq. (B1) as

$$\beta P = \frac{4\eta}{\pi\sigma^2}\left[1 - \frac{1}{2N}\sum_i \sum_{j:j\neq i} \langle (\mathbf{r}_{ij} \cdot \hat{e})(\beta \mathbf{F}_{ij} \cdot \hat{e}) \rangle\right]. \tag{B2}$$

Suppose the active particle $i$ is moving along a direction $\hat{e}$, then the event rate for $i$ to collide with particle $j$ is $q_{ij} = (-\beta \mathbf{F}_{ij} \cdot \hat{e})^+$. The virial formula can be interpreted in terms of ECMC:

$$\begin{aligned}\beta P &= \frac{4\eta}{\pi\sigma^2}\left[1 - \frac{1}{N}\sum_i \sum_{j:j\neq i} \langle (-\mathbf{r}_{ij} \cdot \hat{e})(-\beta \mathbf{F}_{ij} \cdot \hat{e})^+ \rangle\right] \\ &= \frac{4\eta}{\pi\sigma^2}\left[1 + \frac{1}{N}\sum_i \sum_{j:j\neq i} \langle (\mathbf{r}_{ij} \cdot \hat{e}) q_{ij} \rangle\right].\end{aligned} \tag{B3}$$

This equation can be explained in terms of ECMC:

$$\beta P = \frac{4\eta}{\pi\sigma^2}\left[1 + \left\langle \frac{1}{l_{\text{chain}}} \sum_{\text{eventsinchain}} \mathbf{r}_{ij} \cdot \hat{e} \right\rangle_{\text{chain}}\right]. \tag{B4}$$

## APPENDIX C: CLUSTER SIZE

To understand the phase behavior in this work, we analyze the clustering of the particles. In this context, if two neighboring particles are attracted when their patches contact, we say that they are connected by a bond. Two particles are in the same cluster if they can reach each other by a path of bonds. The size of a cluster is the number of particles inside this cluster. And the average cluster size of a system is defined as follows: For a randomly chosen particle, the average size

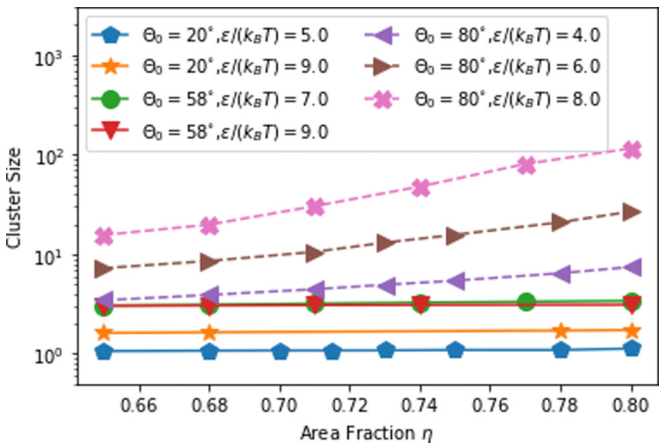


FIG. 13. Cluster sizes.

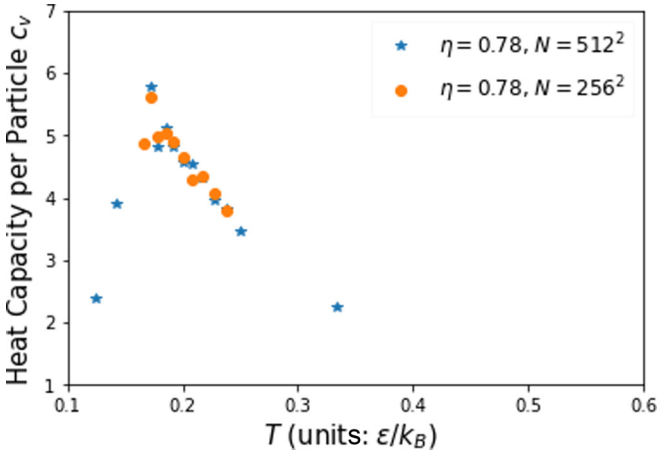


FIG. 14. Constant volume heat capacity per particle $[C_V/(Nk_B)]$ vs temperature $T$ for $\theta_0 = 80^\circ$ at $\eta = 0.78$.

of the cluster containing this particle. Suppose the number of clusters with size $s$ is $N_s$, then the average cluster size is

$$S = \frac{\sum_s s^2 N_s}{\sum_s s N_s}. \tag{C1}$$

The average cluster size for $\theta_0 = 20°$, $\theta_0 = 58°$, and $\theta_0 = 80°$ are shown in Fig. 13.

We can see that for $\theta_0 < 30°$ ($\theta_0 = 20°$), the average cluster size is up to 2. And for $30° < \theta_0 < 60°$, the average cluster size is around 3, and there is no significant increase with temperature decreases. For $60° < \theta_0 < 90°$, the average cluster size increases significantly with reducing temperature.

## APPENDIX D: HEAT CAPACITIES FOR $\theta_0 < 90°$

We show a heat capacity plot for $\theta_0 = 80°$ at $\eta = 0.78$ in Fig. 14. Because it takes a long time to get a smoother result, the statistical fluctuations in the plot are not reduced yet. But it is obvious that there is a sharp peak on each curve around $T \approx 0.179\epsilon/k_B$.


[1] A. Walther and A. H. Muller, Chem. Rev. **113**, 5194 (2013).
[2] P. K. Ghosh, V. R. Misko, F. Marchesoni, and F. Nori, Phys. Rev. Lett. **110**, 268301 (2013).
[3] S. Jiang, J. Yan, J. K. Whitmer, S. M. Anthony, E. Luijten, and S. Granick, Phys. Rev. Lett. **112**, 218301 (2014).
[4] A. Tsyrenova, K. Miller, J. Yan, E. Olson, S. M. Anthony, and S. Jiang, Langmuir **35**, 6106 (2019).
[5] Y. Zhang, F. Jia, L. Tang, P. Zhou, B. Jiang, F. Liang, and Z. Yang, Macromol. Rapid Commun. **40**, 1900067 (2019).
[6] Q. Chen, J. K. Whitmer, S. Jiang, S. C. Bae, E. Luijten, and S. Granick, Science **331**, 199 (2011).
[7] F. Sciortino, A. Giacometti, and G. Pastore, Phys. Rev. Lett. **103**, 237801 (2009).
[8] H. Shin and K. S. Schweizer, Soft Matter **10**, 262 (2014).
[9] K. Mitsumoto and H. Yoshino, Soft Matter **14**, 3919 (2018).
[10] A. Patrykiejew and W. Rżysko, Physica A **548**, 123883 (2020).
[11] T. Huang, Y. Han, and Y. Chen, Soft Matter **16**, 3015 (2020).
[12] J. M. Kosterlitz and D. J. Thouless, J. Phys. C **6**, 1181 (1973).
[13] B. I. Halperin and D. R. Nelson, Phys. Rev. Lett. **41**, 121 (1978).
[14] D. R. Nelson and B. I. Halperin, Phys. Rev. B **19**, 2457 (1979).
[15] A. Young, Phys. Rev. B **19**, 1855 (1979).
[16] S. Chui, Phys. Rev. B **28**, 178 (1983).
[17] E. P. Bernard and W. Krauth, Phys. Rev. Lett. **107**, 155704 (2011).
[18] S. C. Kapfer and W. Krauth, Phys. Rev. Lett. **114**, 035702 (2015).
[19] B. Li, D. Zhou, and Y. Han, Nat. Rev. Mater. **1**, 15011 (2016).
[20] B. Li, F. Wang, D. Zhou, Y. Peng, R. Ni, and Y. Han, Nature (London) **531**, 485 (2016).
[21] Y.-W. Li and M. P. Ciamarra, Phys. Rev. Lett. **124**, 218002 (2020).
[22] D. Frenkel, Science **314**, 768 (2006).
[23] M. Michel, S. C. Kapfer, and W. Krauth, J. Chem. Phys. **140**, 054116 (2014).
[24] P. Bolhuis, M. Hagen, and D. Frenkel, Phys. Rev. E **50**, 4880 (1994).
[25] P. Bolhuis and D. Frenkel, Phys. Rev. Lett. **72**, 2211 (1994).
[26] P. Bladon and D. Frenkel, Phys. Rev. Lett. **74**, 2519 (1995).
[27] N. Kern and D. Frenkel, J. Chem. Phys. **118**, 9882 (2003).
[28] G. Pawley, K. Bowler, R. Kenway, and D. Wallace, Comput. Phys. Commun. **37**, 251 (1985).
[29] J. E. Mayer and W. W. Wood, J. Chem. Phys. **42**, 4268 (1965).